A Chip-Scale Oscillation-Mode Optomechanical Inertial Sensor Near the Thermodynamical Limits

Yongjun Huang, Jaime Gonzalo Flor Flores,* Ying Li, Wenting Wang, Di Wang, Noam Goldberg, Jiangjun Zheng, Mingbin Yu, Ming Lu, Michael Kutzer, Daniel Rogers, Dim-Lee Kwong, Layne Churchill, and Chee Wei Wong**

Modern navigation systems integrate the global positioning system (GPS) with an inertial navigation system (INS), which complement each other for correct attitude and velocity determination. The core of the INS integrates accelerometers and gyroscopes used to measure forces and angular rate in the vehicular inertial reference frame. With the help of gyroscopes and by integrating the acceleration to compute velocity and distance, precision and compact accelerometers with sufficient accuracy can provide small-error location determination. Solid-state implementations, through coherent readout, can provide a platform for high performance acceleration detection. In contrast to prior accelerometers using piezoelectric or capacitive readout techniques, optical readout provides narrow-linewidth high-sensitivity laser detection along with low-noise resonant optomechanical transduction near the thermodynamical limits. Here an optomechanical inertial sensor with an 8.2 μg $Hz^{-1/2}$ velocity random walk (VRW) at an acquisition rate of 100 Hz and 50.9 μg bias instability is demonstrated, suitable for applications, such as, inertial navigation, inclination sensing, platform stabilization, and/or wearable device motion detection. Driven into optomechanical sustained-oscillation, the slot photonic crystal cavity provides radio-frequency readout of the optically-driven transduction with an enhanced 625 μg Hz^{-1} sensitivity. Measuring the optomechanically-stiffened oscillation shift, instead of the optical transmission shift, provides a 220× VRW enhancement over pre-oscillation mode detection.

1. Introduction

Laser-cooled atoms and quantum interferometry has provided new advances in precision measurements of fundamental constants,[1] time,[2] forces,[3] gravity,[4,5] gravitational red-shift,[6] and inertial sensing.[7] In parallel, recent advances in radiation-pressure driven cavity optomechanics[8,9] have provided new frontiers for laser cooling of mesoscopic systems,[10–12] chip-scale stable radio frequency (RF) sources,[13–15] phonon lasers,[16] induced-transparency through multi-mode interferences,[17,18] chaos generation and transfer,[19,20] and explorations into potential quantum transductions of microwave, spin, and optical qubits.[21,22] In cavity optomechanics, the optical cavity and mechanical resonator are co-designed to achieve large optomechanical coupling and transduction.[9,23] This optomechanical transduction is described by the optomechanical coupling coefficient $g_{om}/2\pi$—a shift of the optical frequency ω_o per unit motional displacement x, or equivalently $d\omega_o/dx$. With carefully-tuned high-quality optical factor (Q_o) and tight sub-wavelength confinement of selected optical cavity modes, the induced radiation pressure or optical gradient force can modify or drive the motion of micromechanical resonators.[8,9] As a consequence, a change in optical gradient force also modifies the effective micromechanical resonance frequency. The coupled optical and mechanical degrees-of-freedom[24] allow detections of

Dr. Y. Huang
School of Information and Communication Engineering
University of Electronic Science and Technology of China
Chengdu 611731, China
E-mail: yongjunh@uestc.edu.cn

Dr. Y. Huang, J. G. Flor Flores, Dr. W. Wang, Prof. C. W. Wong
Fang Lu Mesoscopic Optics and Quantum Electronics Laboratory
University of California
Los Angeles, CA 90095, USA
E-mail: jflorflores@ucla.edu; cheewei.wong@ucla.edu

The ORCID identification number(s) for the author(s) of this article can be found under https://doi.org/10.1002/lpor.201800329

DOI: 10.1002/lpor.201800329

Dr. Y. Huang, Dr. Y. Li, D. Wang, N. Goldberg, Dr. J. Zheng, Prof. C. W. Wong
Optical Nanostructures Laboratory
Columbia University
New York, NY 10027, USA

Prof. M. Yu, Prof. D.-L. Kwong
Institute of Microelectronics
A*STAR
Singapore 117865

Prof. M. Lu
Brookhaven National Laboratory
Upton, NY 11973, USA

Dr. M. Kutzer, D. Rogers, L. Churchill
Johns Hopkins Applied Physics Laboratory
Laurel, MD 20723, USA

nanomechanical motion[25,26] toward force sensing,[27] radio wave detection,[28] and magnetic susceptibility measurements.[29]

In the past several years, high-performance micro-accelerometers based on cavity optomechanics have been remarkably advanced for acceleration sensing at higher frequencies above 100 Hz for vibration or shock measurements. Such examples include nanobeam cavities at 10 μg $Hz^{-1/2}$ (1 g = 9.81 m s^{-2}) resolution (sensing bandwidth 5 to 25 kHz) with lock-in detection,[30] cantilevered whispering gallery mode spherical silica cavities at 4.5 μg $Hz^{-1/2}$ resolution (sensing bandwidth 10 to 100 Hz),[31] and bulk fiber-optic cavities at 100 ng $Hz^{-1/2}$ resolution (sensing bandwidth 1 to 10 kHz).[32,33] More details about the accelerometers performance comparisons are described in Supporting Information I. Optomechanical accelerometers with external piezoelectric stages and calibration have also been tested with outdoor operation.[34–37] Unlike these previously demonstrated optomechanical accelerometers, here we demonstrate a new transduction mechanism which is not based on the optical readout through measuring the shift or broadening of optical resonances via dispersive and dissipative optomechanical coupling.

Alternatively, we measure the optomechanically-stiffened oscillation shift instead, which translates into a mechanical frequency shift. This technique generates advantages such as a larger signal-to-noise ratio to suppress the flicker noise and better oscillation frequency shift tracking precision that contributes to improved resolution. In this paper, an oscillation-mode optomechanical inertial sensor with 8.2 μg $Hz^{-1/2}$ velocity random walk (VRW) at an acquisition rate of 100 Hz and 50.9 μg bias instability is demonstrated. Driven by an optically-induced gradient force, our tight sub-wavelength confinement in the photonic crystal cavity[38] allows for a large optomechanical transduction coefficient ($g_{om}/2\pi$)[23] while allowing concurrently a large motional mass for precision sensing. Driven into optomechanical sustained-oscillation and measuring the RF shift instead of the optical resonance, the slot photonic crystal cavity provides RF readout of the optically-driven transduction with enhanced 625 μg Hz^{-1} sensitivity, and a 220× VRW enhancement over pre-oscillation mode detection; all of this due to the strong optomechanical transduction and readout in the optical domain. Our optomechanical inertial sensor operates 2.56× above the thermodynamical limit from 10 to 100 ms with a non-flat noise density, with a 43-dB dynamic range in a solid-state room-temperature vacuum (≈10^{-6} torr) architecture, and is supported by our theory and numerical modeling.

2. Results

2.1. Design of a Laser-Driven RF-Readout Optomechanical Inertial Sensor

The mechanism of our inertial sensor is based on a laser-driven silicon photonic crystal cavity as shown in **Figure 1**a, with one side of the cavity on a stationary beam and the other side of the cavity on a large motional mass. When an acceleration is applied to the motional mass, the slot width s is perturbed, shifting the optical resonance frequency and changing the detuning from the drive laser frequency. This perturbs the intracavity optical energy and hence the optomechanical stiffening (detailed below in Equation (1)). The resulting shifted RF resonance frequency is subsequently read out with high precision, close to the thermodynamical limits.

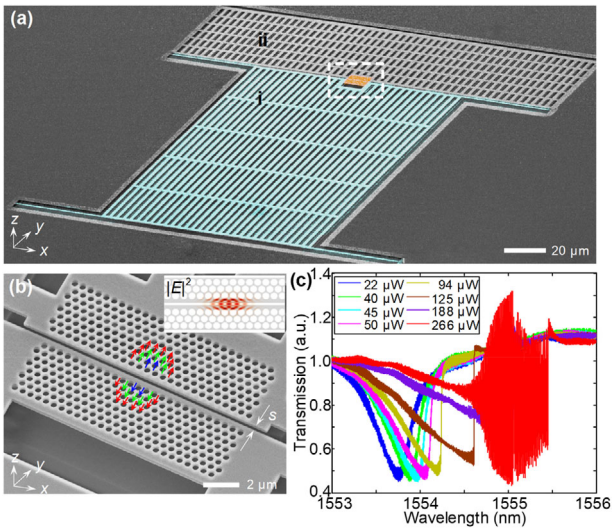

Figure 1. A chip-sale optomechanical inertial sensor. a) Scanning electron micrographs (SEMs) of inertial sensor nanofabricated in silicon-on-insulator (250 nm device layer) with a 5.6 ng proof mass and codesigned slot-type photonic crystal cavity with a slot width s of 80 nm. The fundamental mechanical resonance is designed around 60 to 85 kHz, above most of the ambient, acoustic, and seismic vibrational noise frequencies. Section (i) (in cyan) is the moving mass and section (ii) (in grey) is the stationary section. Scale bar: 20 μm. The orange region is the slot-type photonic crystal cavity, with the dashed white box expanded in panel b. b) Colored arrows denote the 5 nm (red), 10 nm (green), and 15 nm (blue) photonic crystal lattice perturbations to form the slot-localized resonance modes with $0.051(\lambda/n)^3$ mode volumes. Scale bar: 2 μm. Inset: computed $|E|^2$-distribution for the designed nanocavity. c) Optical transmission spectra of the inertial sensor, with increasing drive and readout powers (22 to 266 μW) including observations of self-induced regenerative oscillations with the signature spectral fluctuations (in red).

The optomechanical inertial sensor consists of a slot-type photonic crystal cavity, as illustrated in Figure 1b, nanofabricated in a silicon-on-insulator substrate with a 250 nm thick silicon layer (see Section 5). The cavity is formed by shifted and perturbed lattice holes[23,38] designed to form the localized optical resonant modes as well as an optomechanical gradient force transduction (Supporting Information II.A). The slot cavity features a slot width of s = 80 nm, holes with a radii of r = 150 nm, and lattice constant of a_{pc} = 470 nm, with lattice perturbations of 5 nm (red), 10 nm (green), and 15 nm (blue) to form the localized cavity modes on a line-defect waveguide with width of $1.2 \times \sqrt{3}a_{pc}$. The cavity mode volume is subwavelength at $0.051(\lambda/n)^3$. The large (≈120 μm × 150 μm) proof mass of m_x = 5.6 ng for acceleration detection has four (1 μm × 50 μm) compliant support beams providing a fundamental mechanical resonance of $\Omega_m \approx 2\pi \times$ 71.3 kHz and a combined stiffness of $k \approx 1.12$ N m^{-1}. One side of the slot cavity is attached to this mass and named as section (i) in Figure 1a. The other side (ii) of the slot cavity is cantilevered to the substrate and has the same x-length as the proof mass to reduce

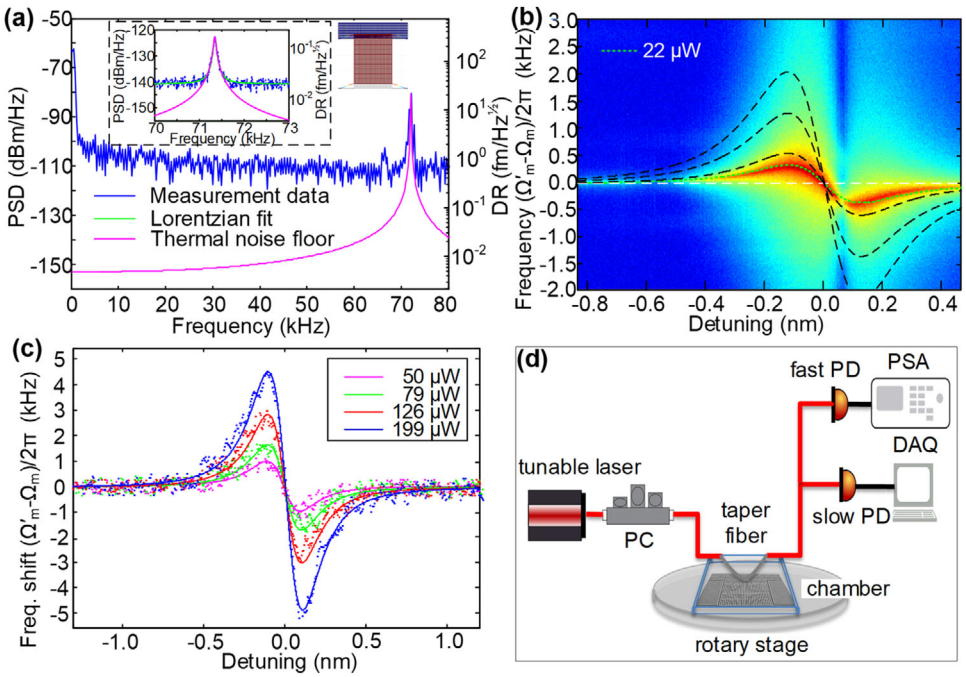

Figure 2. Inertial sensor transduction and enhanced sensitivity in the RF domain. a) Optical gradient force backaction transduction into the RF power spectral density (resolution bandwidth [RBW] of the spectrum analyzer is set as 100 Hz) for the first fundamental mechanical mode at 71.3 kHz with the modeled displacement profile in the right inset. The converted power spectral density in displacement noise unit is shown on the right *y*-axis, with the modeled thermal noise contributions. Left inset is the Lorentzian fit for the zoomed-in fundamental mode (RBW is 1 Hz), which indicates the $Q_m \approx 1383$. b) 2D map of the transduction and optomechanical spring effect in the inertial sensor. The wavelength resolution is 2 pm on a 1552.833 nm optical resonance, at 22 μW input power. The dashed lines show the numerical modeling of the backaction transduction for different laser-cavity detunings, with the green middle line at 22 μW input and the others at 40, 89, and 142 μW, respectively. c) Measured RF shifts (Lorentzian-fitted peaks) for different laser-cavity detunings under several drive powers. Data points are illustrated, with the solid lines from the numerical modeled frequency shifts. d) Measurement setup schematic with dual-detectors for RF tracking and simultaneous optical power monitoring. Optical drive and readout are coupled through tapered fiber coupling. Devices are placed in a vacuum chamber ($\approx 10^{-6}$ torr) on a rotary stage.

asymmetric residual stress *z*-bow between the two sections (i and ii), in order to preserve the localized optical resonance mode.

2.2. Basic Characterizations of the Optomechanical Inertial Sensor at Zero-Acceleration

Initially the performance of the designed optomechanical inertial sensor with large proof mass is demonstrated and characterized at a zero-acceleration condition. Probed by a dimpled tapered fiber anchored to side (ii) of the optomechanical cavity, Figure 1c shows the measured optical transmission spectra under different driving powers. Under a low-driving power (22 μW), the loaded cavity quality factor Q_o is measured at ≈4350 (intrinsic cavity Q_{in} at ≈13200). With increasing driving power, thermal nonlinearity broadens the cavity resonances into asymmetric line-shapes. With optical pump powers greater than 188 μW, the optomechanical cavity is driven into self-induced regenerative oscillations[13]—with significantly narrower mechanical oscillation linewidths and signature spectral fluctuations (shown in red of Figure 1c).

The mechanical motion of the proof mass in the optomechanical inertial sensor (section (i) in Figure 1a), excited by the optical gradient force through strong optomechanical transduction, is recorded by using a fast optical detector and a spectrum analyzer (see Section 5). **Figure 2**a shows an example RF power spectrum, with the optical transmission simultaneously monitored using dual photodetectors, illustrating the fundamental mechanical resonance of 71.3 kHz for the proof mass; the corresponding modeled displacement field profile is shown in the right inset as well (and detailed in Supporting Information II.A). The higher-order excited modes of 2.95 and 4.10 MHz are also found in a larger RF band, as seen in Figure S4, Supporting Information II.C. The left inset of Figure 2a shows the Lorentzian curve fitting, which shows a vacuum (10^{-6} torr) mechanical quality factor Q_m at ≈1383, for the fundamental mode; this is largely bounded by the large proof mass and anchor losses. The proof mass displacement is described by $x(\Omega) = (\Omega_m{}^2 - \Omega^2 + i\,\Omega\Omega_m/Q_m)^{-1} \times a(\Omega) = \chi(\Omega) \times a(\Omega)$ when subjected to an external low-frequency acceleration and thermal noise: $a(\Omega) = a_o(\Omega) + a_{dc} + a_{th}$ in the low frequency regime ($\Omega \ll \Omega_m$), $\chi(\Omega) = 1/\Omega_m{}^2$. The right *y*-axis of Figure 2a and its inset also show the corresponding power spectral density in displacement noise units (detailed in Supporting Information II.C), reaching a displacement noise floor of ≈0.2 fm $Hz^{-1/2}$.

In the slot-type optomechanical cavity, resonant enhancement of the pump-laser optical gradient force yields strong backaction,

and due to the deeply sub-wavelength confinement, the optomechanical stiffening and optical-RF resonance spectra of the cavity are strongly dependent on the slot width s.[23] In the presence of an (+γ direction) acceleration, side (i) of the membrane of the slot cavity shifts with displacement x_s, decreasing the slot width s. Consequently, the optomechanical stiffening increases with a resulting increasing RF resonant frequency Ω'_m (which is theoretically analyzed and numerically modeled at Supporting Information II.B) described by

$$\Omega'_m = \sqrt{\Omega_m^2 + \left(\frac{2|\hat{a}|^2 g_{om}^2}{\Delta^2 \omega_c m_x}\right)\Delta_o}$$
$$= \sqrt{\Omega_m^2 + \left(\frac{2|\hat{a}|^2 g_{om}^2}{((\omega_l - \omega_c + g_{om}x_s)^2 + (\Gamma/2)^2)\omega_c m_x}\right)(\omega_l - \omega_c + g_{om}x_s)} \quad (1)$$

where Ω'_m (Ω_m) is the shifted (unperturbed) RF resonance frequency, $|\hat{a}|^2$ the averaged intracavity photon energy, g_{om} the optomechanical coupling rate, m_x the effective mass, and $\Gamma = 1/\tau$ and ω_c, the optical cavity decay rate and optical resonance frequency, respectively. A linearized form of this equation is also shown in Supporting Information II.B.

From the (x_s to Ω'_m) transfer function in Equation (1), we also note the strong dependence of the mechanical power spectra on the optical cavity resonance, intracavity energy, laser detuning $\Delta_o|_{xs=0} = \omega_l - \omega_0$ and $\Delta^2|_{xs=0} = \Delta^2{}_o + (\Gamma/2)^2$, which enhances the minimal displacement and acceleration sensitivity detection. In addition, we can experimentally monitor the mechanical power spectra under different laser detuning when there is no external acceleration acting on the optomechanical inertial sensor. Figure 2b illustrates the measured 2D RF power spectra with a swept pump wavelength, for the test case of a static (non-acceleration, $x_s = 0$) frame. For the current case, the inertial sensor's optical resonance is 1552.83 nm at a 22 μW incident power with a 50 aJ optical intracavity energy (yielding an intracavity photon number of ≈425) at zero optical detuning. The modeled mechanical frequency for different laser detuning (using Equation (1)) is also superimposed on the 2D measurement. From the measurement-modeling correspondence, we obtain the optomechanical coupling rate to be $g_{om}/2\pi = 37.1$ GHz nm^{-1} (see Supporting Information II.D), with a vacuum optomechanical coupling rate $g^*/2\pi = 180$ kHz. We observe that the RF resonance has a strong optical resonance dependence in the detuning range of $\Delta_o = \pm 0.2$ nm (correlated with the slot width s), with a largest mechanical resonance frequency shift $\Delta\Omega_m/2\pi$ of 450 Hz over an externally-driven 70 pm wavelength detuning. We note that the measured $g_{om}/2\pi$ is smaller than theoretical prediction due to elevation asymmetries of the released masses (sections (i) and (ii) in Figure 1a), lowering the optomechanical transduction from design values (see Figure S3a, Supporting Information II.B). Also, with increased injected optical power, the RF shift range is enhanced due to the stronger optical gradient force as illustrated in Figure 2b,c and detailed in Supporting Information II.B and II.D, resulting in larger slope and better sensitivity when subjected an external acceleration.

2.3. Optomechanical Inertial Sensor Operation in Pre-Oscillation Mode

To measure the RF shift $\Delta\Omega_m$ under low-frequency motion, we fixed the driving wavelength and the driving power (with laser instabilities less than ± 166 fm and ± 0.0017 dB in 10 min), and mounted the device and vacuum setup onto a high-torque Aerotech ADRS-200 rotary stage. This is shown in Figure 2d and detailed in Supporting Information III.A. With optimized digital control and drive filter parameters (detailed in Section 5), the rotary stage provides a noise-equivalent input low-frequency (≈20 Hz) acceleration precision down to sub-μg (in the +γ-axis direction; smaller slot width). **Figure 3**a shows the measured back-action RF transduction in the pre-oscillation mode at 40 μW drive power with $\Omega_m/2\pi \approx 71.5$ kHz in this measurement (Device A). Examining the Lorentzian RF line-shapes over the first 40 spectra (each waveform corresponds to an increase in the applied acceleration up to 154.8 mg) and the theoretical modeling (detailed in Supporting Information IV), the RF frequency is observed to increase by 56.5 Hz on average over the measurement range, equivalent to a sensitivity S of 2.62 ± 0.31 mg Hz^{-1} (or a scale factor of 381.5 ± 45 Hz g^{-1}).

The minimum detectable low-frequency acceleration for the optomechanical inertial sensor has the well-known definition as $a_{min} = S \times \delta\Omega_{rms}/2\pi$,[39,40] where $\delta\Omega_{rms}/2\pi$ is the RMS frequency variation in a specific data acquisition rate, corresponding to the integration time. For a 100 Hz acquisition rate applicable for most of the consumer electronics,[39] $\delta\Omega_{rms}/2\pi$ is determined to be 6.9 Hz (Supporting Information V). This corresponds to a minimum acceleration noise floor, or the resolution of our optomechanical inertial sensor, of ≈1.8 ± 0.21 mg Hz$^{-1/2}$, in pre-oscillation mode. Figure 3e illustrates the measured bias instability and VRW noise of ≈5.23 mg and 1.8 mg Hz$^{-1/2}$, respectively, which are the two very important parameters indicating the minimum achievable low-frequency acceleration reading limited by flicker noise and the total noise density.[31,33] Figure 3f shows the converted acceleration power spectrum density (PSD) which indicates the non-flat noise density in the low frequency range from 0.001 to 20 Hz. Theoretically, in pre-oscillation mode, the thermal noise frequency fluctuation is given by:[41,42] $\delta\Omega_{th} = [(k_B T/E_C) \times (\Omega_m \Delta f/Q_m)]^{1/2}$, from the measured power spectra density and with Δf the acquisition rate corresponding to the integration time, and $E_C = m_x \Omega_m{}^2 \langle x_c{}^2 \rangle$ the energy in the carrier in the oscillator and $\langle x_c \rangle$ the constant mean square amplitude. With a signal-to-noise ratio (SNR = 10log($E_C/k_B T$)) of ≈18 dB and Q_m of 1383, we obtain $\delta\Omega_{th}/2\pi$ as 9.04 Hz in 0.01 second integration time. Correspondingly, with the sensitivity of 1.1 mg Hz^{-1} for the optimized optical detuning, this gives a theoretically-estimated acceleration resolution $R \approx 995$ μg Hz$^{-1/2}$ (detailed in Supporting Information VI.A), in pre-oscillation mode. The theoretical thermodynamical acceleration noise floor with optimized optical detuning closed to the optical resonance is also presented in Figure 3f. The excess noises shown in the measurements, with the acceleration PSD non-flat at the low-frequency region, are mainly from system noise such as the laser frequency noise, parasitic displacement noise, device thermal fluctuation, and thermal expansion noise among others.[33] We note that only the first 40 RF spectra (up to 154.8 mg) are used in the analysis to be well within the linear dynamic range (<0.05% standard

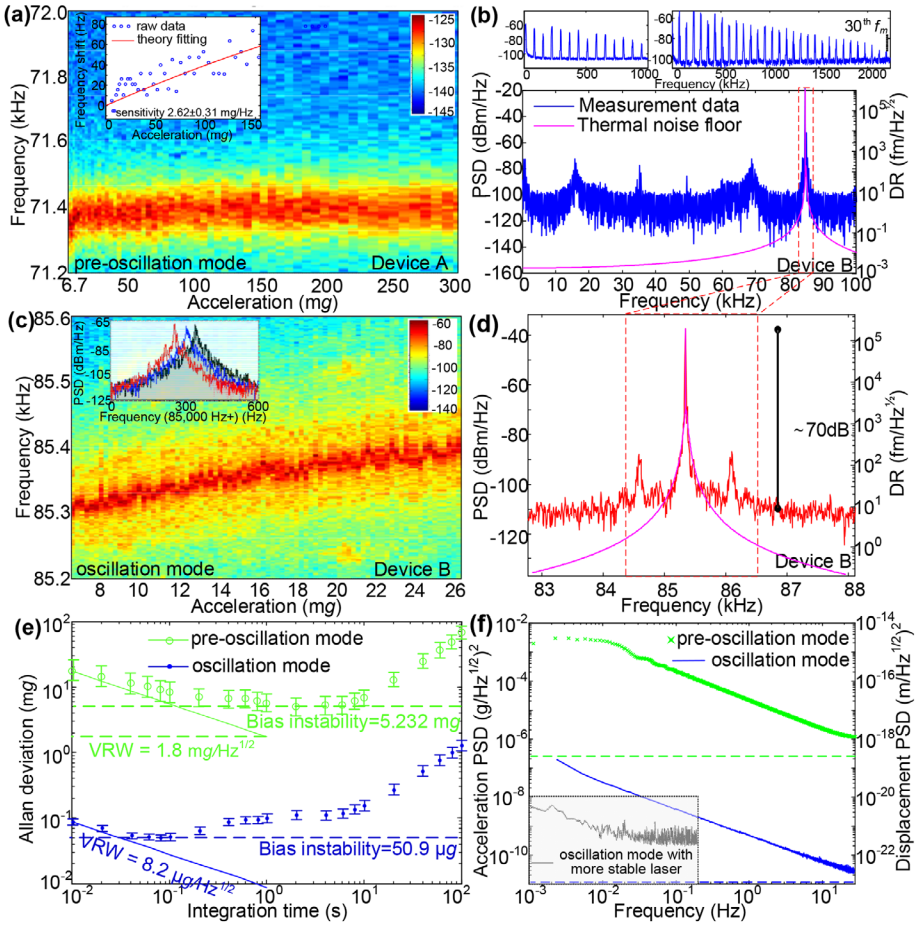

Figure 3. Acceleration signal detection. a) Backaction RF transduction at 40 μW drive power under different accelerations, from 6.7 to 300 mg. Accelerations applied on the device (Device A) pointing outward from rotation center. Mechanical RF frequency increases by 146 Hz. Inset shows the Lorentzian fitted resonance frequency shift for increasing acceleration, with modeled solid curve. The overall fit to the detection sensitivity is at 2.62 ± 0.31 mg Hz^{-1}. b) Inertial sensor driven into self-sustained oscillation mode (Device B), with optical drive power exceeding the intrinsic mechanical damping, with up to 30th harmonic observed (top panel). c) Tracked mechanical power spectra of oscillation-mode acceleration sensing at ≈200 μW drive power. Accelerations applied are from 6.5 to 26.3 mg pointing outward from rotation center, with device mounted with reduction of slot width *s*. Mechanical resonance frequency increases by ≈31.7 Hz. Top inset: comparison RF spectra under 6.53, 14.68, and 26.34 mg (from left to right), respectively. d) Zoomed-in image of fundamental oscillation mode at 85.3 kHz in this device, with the sidebands arising from coupling to out-of-plane modes. e) Overall Allan deviation in terms of acceleration ($= S \times \sigma(\tau) \times \Omega_m/2\pi$,[30,32] where $\sigma(\tau)$ is the Allan deviation shown in Figure S7a, Supporting Information, of the inertial sensor at pre-oscillation and oscillation modes. The obtained bias instability and velocity random walk are estimated, respectively, from the −1/2 slope and zero slope for both modes. f) Pre-oscillation and oscillation modes acceleration PSD data. The definition used for the calculation of the PSD is the Fourier transforms of the autocorrelation function of the measured data. The dashed green and blue lines correspond to the thermal noise floors at optimized optical detuning retrieved from Figure S8, Supporting Information. The inset shows low-frequency noise reduction based on the more stable laser source.

deviation). We also measured other inertial sensor devices in our setup with similar geometries, including an inertial sensor mounted 180° opposite from Figure 3a (i.e., acceleration in the $-y$-axis direction); the mechanical resonance frequency shift is observed in opposite direction under the same acceleration ranges as detailed in Supporting Information III.B.

2.4. Optomechanical Inertial Sensor Operation in Oscillation Mode

Next we drove the 5.6 ng optomechanical inertial sensor into oscillation mode as shown in Figure 3b–d, with driving powers above 188 μW. From the nonlinear optomechanical transduction, high-order harmonics (up to the 30th harmonic) of the fundamental resonance are observed above threshold,[9] with two example spectra shown in the top insets of Figure 3b. In this device (Device B), the fundamental oscillation frequency is 85.3 kHz, with the sidebands arising from coupling to out-of-plane modes (see Figure 3d). Note the ≈70 dB intensity peak-to-noise floor when in the self-induced regenerative oscillation regime, compared to ≈18 dB in the resonant (pre-oscillation) mode. Figure 3c illustrates the tracked RF shift under 6.53 to 26.34 mg low-frequency accelerations, with ≈200 μW intracavity driving power. We note the sizably larger RF shift at ≈31.7 Hz, compared to the pre-oscillation regime, even when measured over ≈11 × smaller low-frequency acceleration ranges as compared to Figure 3a. The

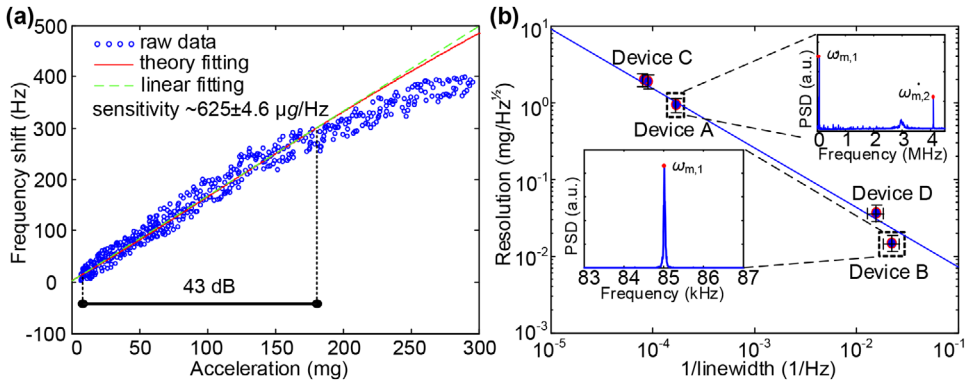

Figure 4. Oscillation mode sensitivity and resolution enhancement. a) Lorentzian-fitted oscillation frequency shift for increasing acceleration, with modeled solid curve. Dashed line is the linear fit, indicating the measured dynamic range as 43 dB and theoretical dynamic range as 44.8 dB. b) Summary of resolution versus optomechanical cavity linewidth. Four independent devices are measured in this panel, with one repeated device (Device C) for different pump conditions. Devices A and C are operating at pre-oscillation mode; and Devices B and D are in oscillation mode. Inset: power spectral density of the investigated modes (Devices A and B, already characterized in details in the main text).

inset of Figure 3c illustrates the spectra comparison (left to right) under 6.53, 14.68, and 26.34 mg, respectively. To characterize the oscillator, we also measured the frequency instability of our optomechanical inertial sensor, as detailed in Supporting Information V. This shows an Allan deviation of 3.8×10^{-6} fractional frequency instability at 10 ms integration. **Figure 4**a shows the oscillation mode acceleration measurement data, with the datapoints obtained from Lorentzian RF peak detection. The fitted oscillation frequency shift dependence shows a detection sensitivity S of 625 ± 4.6 μg Hz^{-1} (or equivalently, a scale factor of 1.6 ± 0.012 kHz g^{-1}). The improved sensitivity is due to the larger slope as shown in Figure 2b,c, resulting from the higher drive power ($|\hat{a}|^2$ in Equation (1)). This matches our theoretical modeling predictions (detailed in Supporting Information IV for both pre-oscillation and oscillation modes).

The obtained minimum acceleration noise floor in oscillation mode, based on the measured oscillator sensitivity and long-term frequency instability (detailed in Supporting Information V), is determined to be ≈8.2 ± 0.07 μg $Hz^{-1/2}$ in the acquisition rate of 100 Hz, and from low integration times of 10 to 100 ms. We emphasize that this is ≈220 × better than the pre-oscillation mode. Figure 3e also shows the determined bias instability of ≈50.9 μg in oscillation mode and Figure 3f indicates the converted acceleration PSD also with non-flat noise density across the frequency band from 0.001 to 20 Hz. With more stable laser source, the low-frequency noise can be reduced more than an order-of-magnitude at the 0.001 Hz frequency point and half an order-of-magnitude at the 0.01 Hz frequency point. Consequently, we reached a flat noise floor of 19.5 μg $Hz^{-1/2}$ for a frequency range between 0.03 to 0.2 Hz, and as noted by the data, the noise floor can be further shaped to be flat in a wider range at low frequencies. In addition to the ± 4.6 μg Hz^{-1} sensitivity regression estimate, the long-time (1 h timescale) standard deviation of the frequency shift fluctuations $\delta\Omega/2\pi$ is also analyzed to be 9.78 Hz. It should be noticed that VRW is mostly related to thermal effects, and it provides a measure of these as seen by the system. At the same time, bias instability is one of the most important parameters when constant acceleration is measured for inertial navigation. In oscillation mode, we also note that the large peak-to-noise floor ratio allows a minimal distinguishable oscillation frequency shift (between two overlapping Lorentzian lineshapes) $\delta\Omega_{\mathrm{rms}}$ much smaller than in pre-oscillation.

3. Discussion

Even in pre-oscillation mode, we emphasize that the detectable 3.05 Hz RF shift (Supporting Information VI.B) is equivalent to a 467 fm wavelength perturbation in the optical cavity resonance. Such 3 Hz RF precision detection requirement is much easier than a 467 fm optical frequency shift because the optical setup would require homodyne detection—extra components essentially. This makes our RF readout optomechanical inertial sensor more suitable for compact and low-cost commercial application. For maximal sensitivity to the external low-frequency acceleration, we can further tune the drive and readout laser wavelength to the slot-cavity resonance. The cavity slot direction is aligned perpendicular to the rotation radius, allowing the imparted centrifugal force to be in the ±y-direction onto the proof mass (the alignment error is negligible and, even for a ±5° error, contributes only a ±0.38% fixed offset in the imparted force measurement, as noted in Supporting Information III.B). Furthermore, we note that the estimated instabilities of the driving wavelength (± 166 fm) over 10 min contribute to only a ± 5% uncertainty in the acceleration resolution (derived from Supporting Information III.B); for long-term measurements this uncertainty can be readily improved with more stable drive lasers. We also note that the coupled intracavity power is monitored to account for any coupling drifts or power fluctuations in the rotation measurements, and a polarization-maintaining tapered fiber serves as the input/output coupling fiber through vacuum chamber to avoid any polarization shifts during the imparted rotation and acceleration.

Without optomechanical stiffening, the inertial sensor resolution is solely represented by the mechanical domain parameters and described by thermal Brownian noise (detailed in Supporting Information VI). With the large mass oscillator and high driving powers, the thermal Brownian noise can be largely reduced[41,42]

and then the measured frequency instability and acceleration sensitivity can be strongly improved, resulting in better resolution. The optical noise bound arising from quantum backaction noise a_{BA} [33] is estimated to be ≈184 ng Hz$^{-1/2}$ for our oscillator design and implementation parameters, and is detailed in Supporting Information VI.B. We note that, with this RF transduction readout approach instead of solely the optical intensity transmission readout, optical shot noise, and photodetector shot noise do not contribute significantly to the fundamental limit in our readout scheme, allowing our measured acceleration noise floor to be close to the thermal noise limit.

Figure 4a shows the resulting measured frequency shift $\Delta\Omega_m$ over a large acceleration range. To support the inertial sensor demonstration, we determine the linear dynamic range experimentally from the minimum detectable acceleration (8.2 μg) to ≈170 mg, as 43 dB. This differs from the theoretical design estimate of ≈44.8 dB (detailed in Supporting Information VII) due to fabrication variations and the nonlinear dependence of the optical resonance on the slot width *s*. Figure 4b summarizes the detection resolution versus linewidth, over four independent devices, indicating that better resolution can be achieved with narrower mechanical linewidth. In addition, to further improve the sensitivity and resolution, self-reference noise cancellation[43] or thermal stabilization through multiply-resonant optomechanical oscillators[44] can be pursued. The remaining deviations of the modeled sensitivity from the measurements likely arise from a residual ≈25% over-estimate of the optical resonance shift per displacement in the finite-difference time-domain simulations.

4. Conclusion

We have demonstrated an optomechanical inertial sensor driven into the oscillation mode, for the first time, for enhanced noise-equivalent acceleration measurements. In pre-oscillation mode, the optomechanical drive and readout show a sensitivity of 2.62 mg Hz^{-1}. Driven into self-regenerative optomechanical oscillation modes, the oscillator demonstrates an enhanced acceleration sensitivity of 625 μg Hz^{-1} and a noise floor down to ≈8.2 μg Hz$^{-1/2}$ with 100 Hz data acquisition rate, close to the thermal noise limit (≈3.2 μg Hz$^{-1/2}$) at low integration times from 10 to 100 ms. The mesoscopic room-temperature implementation with RF optomechanical transduction and readout provides a platform toward low-noise precision sensing such as inertial navigation, inclination sensing, and platform stabilization.

5. Experimental Section

Device Nanofabrication: The inertial sensors were fabricated both in the CMOS foundry (Institute of Microelectronics, Singapore) and with electron-beam nanolithography at Brookhaven National Laboratory, USA. The silicon-on-insulator had a 250 nm device thickness on top of a 3 μm buried oxide cladding. The CMOS fabrication is described in ref. [13]. In the electron-beam lithography, an ultrasonicator and O_2 plasma were used to prepare and clean the surface of the wafer before spin-casting 100% ZEP 520A resist on it. Proximity error correction with Layout BEAMER allowed the nanopatterning of the 80 nm (line) slot next to the photonic crystal round holes, with high fidelity to create the photonic crystal nanocavities. The nanocavities were then written with the 50 MHz JEOL JBX-6300FS system at 100 keV, with rigorously optimized base dose of 280 μC cm^{-2}. Numerous variants of the "self-consistent dose correction" were applied to correct proximity effect. The nanopattern was developed in xylene for 90 s. The resulting pattern was then transferred into the silicon device layer through inductively-coupled plasma dry-etching at a rate of 20 nm s^{-1}. The E-beam resist was removed via Microposit solvent 1165 at 90 °C and the large-membrane nanocavities air-bridged via wet-etching the underlying oxide in 5:1 buffered-oxide etchant for 17 min. The samples were released with the critical point drying technique to overcome stiction and to provide high yield.

Experiment Setup: An Aerotech ADRS-200 rotary stage was used to impart a known acceleration onto the optomechanical inertial sensor. This high-torque rotary stage was driven by a brushless servomotor and equipped with direct coupled, high-accuracy rotary encoders. With the Soloist digital scope control, the control filter parameters were set at the optimal gain values (position loop gain k_{pos} = 10, integral gain k_i = 500, and proportional gain k_p = 105 000) to drive the acceleration to the set values rapidly without overtone ringing, with the authors' low rotational velocities and large measurement setup load. The inertial sensor was mounted 21.60 ± 0.01 cm from the axis of rotation on a 5-axis Attocube positioner within a customized Janis ST-500 vacuum chamber. A dimpled tapered fiber with more than 90% transmission was passed through a fiber feedthrough and coupled to the inertial sensor, by anchoring the fiber dimple directly on the chip surface and touching on side (ii) (see Figure 1a) of the optomechanical slot cavity, via strong van der Waals/electrostatic forces. The optical resonance intensity was monitored to ensure the transmission and coupling, which were maintained during the slow rotation. The optical drive was provided by a tunable laser diode (Santec TSL-510) without the conventional Pound-Drever-Hall locking (since optical resonance linewidth is wide), while simultaneous readout of the RF and optical spectra is measured with a balanced photodetector. A high-resolution commercial accelerometer is placed on the opposite side of the rotating stage; however, at low acceleration levels, the accelerometer was always at the noise floor. A polarization controller and a polarization maintaining fiber were employed to maintain the stable drive polarization while the stage was rotating. To obtain the RF transduction under different low-frequency accelerations, a fully-integrated LabVIEW VI was built. The rotating speed of the rotary stage corresponding to the acceleration and the RF PSD collected from the spectrum analyzer were controlled by the VI. The resolution bandwidth (RBW) and video bandwidth (VBW) were specifically controlled in the spectrum analyzer for different data collecting frequency band requirements. For examples, in the acceleration measurement, the narrow RF collecting frequency band (≈ 1 kHz) with 600 datapoints, with RBW of 10 Hz, and VBW of 1 Hz ensures the rapid RF PSD collection.

Numerical Modeling: The coherent optomechanical coupling rate $g^*/2\pi$ was obtained through first-order perturbation theory and computed through the closed-form integrals of the electromagnetic fields and displacement fields of the inertial sensor including the relative permittivity. The optical resonant modes and electromagnetic fields of the photonic crystal cavity were obtained from finite-difference time-domain simulations through a freely available software package (MEEP). Mechanical displacement fields and modes were determined with COMSOL Multiphysics. Coupled mode theory on the optical fields and the harmonic oscillator[38] was used to model the optical stiffening of the RF tone and the dynamical shifts.

Supporting Information

Supporting Information is available from the Wiley Online Library or from the author.

Acknowledgements

Y.H., J.G.F.F., and Y.L. contributed equally to this work. The authors acknowledge discussions with S.-W. Huang, J. Lim, J. F. McMillan, J.

Wu, S. Bhave, P.-C. Hsieh, Z. Xie, W. Wang, and P. Hamilton. The authors acknowledge support from the National Science Foundation (SDC-1520952), Johns Hopkins Applied Physics Laboratory, and the Department of Defense. Research carried out in part at the Center for Functional Nanomaterials, Brookhaven National Laboratory, which was supported by the U.S. Department of Energy, Office of Basic Energy Sciences, under contract number DE-AC02-98CH10886. Y.H. acknowledges the supports from National Natural Science Foundation of China (61701082), National Postdoctoral Program for Innovative Talents (BX201700043), and Sichuan Provincial Science and Technology Planning Program of China (2019YFG0120).

Conflict of Interest

The authors declare no conflict of interest.

Keywords

cavity optomechanics, inertial sensors, optomechanical oscillation

Received: November 29, 2018
Revised: February 10, 2020
Published online: April 8, 2020

[1] G. Rosi, F. Sorrentino, L. Cacciapuoti, M. Prevedelli, G. M. Tino, *Nature* **2014**, *510*, 518.
[2] S. L. Campbell, R. B. Hutson, G. E. Marti, A. Goban, N. Darkwah Oppong, R. L. McNally, L. Sonderhouse, J. M. Robinson, W. Zhang, B. J. Bloom, J. Ye, *Science* **2017**, *358*, 90.
[3] S. Schreppler, N. Spethmann, N. Brahms, T. Botter, M. Barrios, D. M. Stamper-Kurn, *Science* **2014**, *344*, 1486.
[4] N. Malossi, Q. Bodart, S. Merlet, T. Lévèque, A. Landragin, F. P. Dos Santos, *Phys. Rev. A* **2010**, *81*, 013617.
[5] Y. Bidel, O. Carraz, R. Charrière, M. Cadoret, N. Zahzam, A. Bresson, *Appl. Phys. Lett.* **2013**, *102*, 144107.
[6] H. Muller, A. Peters, S. Chu, *Nature* **2010**, *463*, 926.
[7] F. Sorrentino, K. Bongs, P. Bouyer, L. Cacciapuoti, M. de Angelis, H. Dittus, W. Ertmer, J. Hartwig, M. Hauth, S. Herrmann, K. Huang, M. Inguscio, E. Kajari, T. Könemann, C. Lämmerzahl, A. Landragin, G. Modugno, F. P. dos Santos, A. Peters, M. Prevedelli, E. M. Rasel, W. P. Schleich, M. Schmidt, A. Senger, K. Sengstock, G. Stern, G. M. Tino, T. Valenzuela, R. Walser, P. Windpassinger, *J. Phys. Conf. Ser.* **2011**, *327*, 012050.
[8] T. J. Kippenberg, K. J. Vahala, *Science* **2008**, *321*, 1172.
[9] M. Aspelmeyer, T. J. Kippenberg, F. Marquardt, *Rev. Mod. Phys.* **2014**, *86*,1391.
[10] J. Chan, T. P. M. Alegre, A. H. Safavi-Naeini, J. T. Hill, A. Krause, S. Gröblacher, M. Aspelmeyer, O. Painter, *Nature* **2011**, *478*, 89.
[11] Y.-C. Liu, Y.-F. Xiao, X. Luan, C. W. Wong, *Phys. Rev. Lett.* **2013**, *110*, 153606.
[12] G. I. Harris, D. L. McAuslan, E. Sheridan, Y. Sachkou, C. Baker, W. P. Bowen, *Nat. Phys.* **2016**, *12*, 788.
[13] X. Luan, Y. Huang, Y. Li, J. F. McMillan, J. Zheng, S.-W. Huang, P.-C. Hsieh, T. Gu, D. Wang, A. Hati, D. A. Howe, G. Wen, M. Yu, G. Lo, D.-L. Kwong, C. W. Wong, *Sci. Rep.* **2015**, *4*, 6842.
[14] M. Zhang, S. Shah, J. Cardenas, M. Lipson, *Phys. Rev. Lett.* **2015**, *115*, 163902.
[15] Y. Huang, J. Wu, J. G. F. Flores, M. Yu, D.-L. Kwong, G. Wen, C. W. Wong, *Appl. Phys. Lett.* **2017**, *110*, 111107.
[16] K. Vahala, M. Hermann, S. Knünz, V. Batteiger, G. Saathoff, T. W. Hänsch, Th. Udem, *Nat. Phys.* **2009**, *5*, 682.
[17] S. Weis, R. Rivière, S. Deléglise, E. Gavartin, O. Arcizet, A. Schliesser, T. J. Kippenberg, *Science* **2010**, *330*, 1520.
[18] C. Dong, V. Fiore, M. Kuzyk, H. Wang, *Science* **2012**, *338*, 1609.
[19] F. Monifi, J. Zhang, Ş. K. Özdemir, B. Peng, Y. X. Liu, F. Bo, F. Nori, L. Yang, *Nat. Photonics* **2016**, *10*, 399.
[20] J. Wu, S.-W. Huang, Y. Huang, H. Zhou, J. Yang, J.-M. Liu, M. Yu, G. Lo, D.-L. Kwong, S. Duan, C. W. Wong, *Nat. Commun.* **2017**, *8*, 15570.
[21] T. A. Palomaki, J. W. Harlow, J. D. Teufel, R. W. Simmonds, K. W. Lehnert, *Nature* **2013**, *495*, 210.
[22] A. P. Reed, K. H. Mayer, J. D. Teufel, L. D. Burkhart, W. Pfaff, M. Reagor, L. Sletten, X. Ma, R. J. Schoelkopf, E. Knill, K. W. Lehnert, *Nat. Phys.* **2017**, *13*, 1163.
[23] Y. Li, J. Zheng, J. Gao, J. Shu, M. S. Aras, C. W. Wong, *Opt. Express* **2010**, *18*, 23844.
[24] K. C. Balram, M. I. Davanço, J. D. Song, K. Srinivasan, *Nat. Photonics* **2016**, *10*, 346.
[25] M. Li, W. H. P. Pernice, H. X. Tang, *Nat. Nanotechnol.* **2009**, *4*, 377.
[26] G. A. Brawley, M. R. Vanner, P. E. Larsen, S. Schmid, A. Boisen, W. P. Bowen, *Nat. Commun.* **2016**, *7*, 10988.
[27] L. M. de Lépinay, B. Pigeau, B. Besga, P. Vincent, P. Poncharal, O. Arcizet, *Nat. Nanotechnol.* **2017**, *12*, 156.
[28] T. Bagci, A. Simonsen, S. Schmid, L. G. Villanueva, E. Zeuthen, J. Appel, J. M. Taylor, A. Sørensen, K. Usami, A. Schliesser, E. S. Polzik, *Nature* **2014**, *507*, 81.
[29] M. Wu, N. L.-Y. Wu, T. Firdous, F. F. Sani, J. E. Losby, M. R. Freeman, P. E. Barclay, *Nat. Nanotechnol.* **2017**, *12*, 127.
[30] A. G. Krause, M. Winger, T. D. Blasius, Q. Lin, O. Painter, *Nat. Photonics* **2012**, *6*, 768.
[31] Y. L. Li, P. F. Barker, *J. Lightwave Technol.* **2018**, *36*, 3919.
[32] F. G. Cervantes, L. Kumanchik, J. Pratt, J. M. Taylor, *Appl. Phys. Lett.* **2014**, *104*, 221111.
[33] O. Gerberding, F. G. Cervantes, J. Melcher, J. R. Pratt, J. M. Taylor, *Metrologia* **2015**, *52*, 654.
[34] W. T. Pike, A. K. Delahunty, A. Mukherjee, G. Dou, H. Liu, S. Calcutt, I. M. Standley, presented at 2014 IEEE Sensors, Valencia, Spain, November **2014**.
[35] A. E. Stott, C. Charalambous, T. J. Warren, W. T. Pike, *IEEE Sens. J.* **2018**, *18*, 9382.
[36] R. P. Middlemiss, S. G. Bramsiepe, R. Douglas, J. Hough, D. J. Paul, S. Rowan, G. D. Hammond, *Sensors* **2017**, *17*, 2571.
[37] Y. L. Li, P. F. Barker, *Sensors* **2018**, *18*, 4184.
[38] J. Gao, J. F. McMillan, M.-C. Wu, J. Zheng, S. Assefa, C. W. Wong, *Appl. Phys. Lett.* **2010**, *96*, 051123.
[39] C. Comi, A. Corigliano, G. Langfelder, A. Longoni, A. Tocchio, B. Simoni, *J. Microelectromech. Syst.* **2010**, *19*, 1140.
[40] L. Rodriguez-Pardo, J. F. Rodriguez, C. Gabrielli, H. Perrot, R. Brendel, *IEEE Sens. J.* **2005**, *5*, 1251.
[41] K. L. Ekinci, Y. T. Yang, M. L. Roukes, *J. Appl. Phys.* **2004**, *95*, 2682.
[42] X. L. Feng, C. J. White, A. Hajimiri, M. L. Roukes, *Nat. Nanotechnol.* **2008**, *3*, 342.
[43] Y. Zhao, D. J. Wilson, K.-K. Ni, H. J. Kimble, *Opt. Express* **2012**, *20*, 3586.
[44] A. B. Matsko, A. A. Savchenkov, V. S. Ilchenko, D. Seidel, L. Maleki, *Phys. Rev. A* **2011**, *83*, 021801(R).

